AIAA JOURNAL
Vol. 40, No. 3, March 2002

Applications of High-Order Optimized Upwind Schemes for Computational Aeroacoustics

M. Zhuang* and R. F. Chen†
Michigan State University, East Lansing, Michigan 48824

High-order optimized upwind dispersion-relation-preserving finite difference schemes are used for solving multidimensional acoustic wave propagation problems. The accuracy and the robustness of the schemes are tested for acoustic problems with various geometry and boundary conditions. Excellent agreements between the numerical and the analytical solutions indicate that the high-order optimized upwind schemes minimize not only the dispersion error but also the dissipation error while retaining the numerical stability. The simulation results have also demonstrated that the optimized upwind schemes damp out the spurious short waves automatically without the need of filter or explicit dissipation terms. The overall effectiveness of the high-order optimized upwind schemes is verified. The good numerical result of the problem of acoustic scattering by a sphere suggests that the optimized upwind schemes may be used to solve acoustic problems involving a relatively complex geometry.

Introduction

AEROACOUSTIC problems are governed by the same equations as those in aerodynamics, namely, the Navier–Stokes equations. Aeroacoustic problems, however, have their own nature, characteristics, and objectives, which are distinctly different from those commonly encountered in aerodynamics.[1] These characteristics require numerical schemes to have minimum numerical dispersions and dissipations so that the numerically calculated waves can travel with an accurate speed, phase, and amplitude. Many computational fluid dynamics (CFD) schemes, such as the MacCormack scheme, traditional upwind schemes, essentially nonoscillatory (ENO) schemes, etc., have been extended to a higher order using more stencil points and applied to the computation of acoustic problems.[2,3] It has been shown,[4] however, that for waves with large wave numbers (short waves) the optimized schemes, such as the dispersion-relation-preserving (DRP) schemes, require less grid points per wavelength (PPW) than traditional high-order CFD schemes. Because a large computational domain is usually required, the property of requiring less PPW is essential in computational aeroacoustics. Like Tam and Webb's DRP schemes,[4] most of the optimized schemes are based on the central difference schemes that are nondissipative in nature. Spurious oscillations in numerical solutions are generated when there are discontinuities in the flowfield. The elimination of the spurious oscillations must be dealt with through the use of filters or explicit dissipation terms. Although filters or dissipation terms have been proved to be successful in solving many acoustic problems, they are problem dependent. The proper use of these filters or dissipation terms may require the prior knowledge of the problems.

To remedy this problem, wave number-extended high-order upwind schemes have been developed.[5–7] These upwind schemes are optimized in the wave number space following the same idea of central DRP schemes.[4] The main difference among these upwind schemes is the treatment of the imaginary part of the numerical wave number in the optimization process. Upwind schemes have been widely used in CFD and have been shown to be very efficient and robust.[8–10] Upwind schemes not only ensure that waves propagate in correct physical directions, with the built-in dissipation, upwind schemes automatically damp out the spurious waves in a numerical solution. Because the dissipation does not distinguish the spurious waves from actual acoustic waves, upwind schemes need to be optimized so that the effect of dissipation on a large range of acoustic waves is minimized. The objectives of the current investigations are 1) to implement the high-order optimized upwind DRP scheme[7] for multidimensional aeroacoustics problems, 2) to verify the accuracy and the robustness of the optimized scheme by solving a series of acoustic wave propagation problems, and 3) to demonstrate the overall effectiveness of the high-order optimized upwind scheme by comparing the results from the optimized upwind scheme to that of the central DRP scheme and the analytic solutions.

Problem Formulation

Finite difference schemes discretize partial differential equations by approximating and replacing partial differential derivatives with finite differences. The discretizations result in algebraic equations that can then be solved by various well-developed numerical methods. There are basically two ways to discretize the differential equations. One is to treat spatial and temporal derivatives in the differential equations separately. The discretizations of spatial derivatives result in a system of semidiscrete ordinary differential equations, and the temporal derivatives can then be further discretized by a well-developed method such as the Runge–Kutta method, mutistages method, or by optimized time discretizations. The second approach is to approximate the spatial and temporal derivatives simultaneously. No intermediate semidiscrete forms are produced. Classical Lax–Wendroff and MacCormack finite difference schemes belong to the second category. In the current study, the optimized high-order upwind scheme is developed using the first approach. The study is focused on the spatial discretization and the optimization process. The time discretization used in the scheme is the same as that of Tam and Webb.[4]

To simplify the problem, the one-dimensional scalar model wave equation is considered[7]:

$$\frac{\partial u}{\partial t} + c\frac{\partial u}{\partial x} = 0 \tag{1}$$

where c is the propagating speed of the wave. Without the loss of generality, we assume that $c > 0$. The approximation of the first-order spatial derivative $\partial u/\partial x$ by a finite difference on an uniform grid of spacing Δx is given by

$$\left(\frac{\partial u}{\partial x}\right)_l \approx \frac{1}{\Delta x}\sum_{j=-N}^{M} a_j u_{l+j} \tag{2}$$

where a_j are coefficients that are determined according to required order of accuracy and other properties and l is an integer

Received 26 July 2000; revision received 27 July 2001; accepted for publication 21 August 2001.

*Associate Professor, Department of Mechanical Engineering. Member AIAA.

†Graduate Assistant, Department of Mechanical Engineering; currently Project Engineer, Engineering Technology Associates, Inc., Troy, MI 48083.

representing grid node. The fourth-order, seven-point stencil optimized upwind DRP scheme is developed.[7] The two free coefficients a_l ($l=-4, -3$; without the loss of generality, we assume that the coefficients a_{-4} and a_{-3} are free) are used to minimize the integrated error E defined as[7]

$$E = \int_0^{\beta_0} |\bar{\alpha}_r \Delta x - \alpha \Delta x|^2 \, \mathrm{d}(\alpha \Delta x) + \lambda \int_0^{\beta_0} \left| \bar{\alpha}_i \Delta x + \mathrm{sgn}(c) \exp\left[-\ln 2 \left(\frac{\alpha \Delta x - \pi}{\sigma} \right)^2 \right] \right|^2 \mathrm{d}(\alpha \Delta x) \tag{3}$$

where β_0 is a predetermined number that gives the optimized range of wave numbers. The parameter λ is a weighting coefficient and used to balance the L_2 norm of the truncation errors of the approximation of the real and the imaginary parts of the effective numerical wave number $\bar{\alpha}$ to that of the actual wave number α. The necessary conditions used to minimize E are

$$\frac{\partial E}{\partial a_l} = 0, \qquad l = -4, -3 \tag{4}$$

The first term in Eq. (3) minimizes the distance between $\bar{\alpha}_r \Delta x$ and $\alpha \Delta x$ in the form of the L_2 norm. The second term, instead of minimizing the distance between $\bar{\alpha}_i \Delta x$ and 0, minimizes the distance between $\bar{\alpha}_i \Delta x$ and a Gaussian function in the form of L_2 norm, which is almost zero when the value of $\alpha \Delta x$ is far from π. The Gaussian term is chosen such that the imaginary part of the effective wave number $\bar{\alpha}_i \Delta x$ is very close to zero for waves with wave numbers within a certain range. The second term in Eq. (3) also allows controls over short-wave or high-frequency damping by adjusting the control parameter σ.

As in a traditional finite difference scheme, the upwind scheme uses more stencils upwind (from the left) than downwind (from the right) because the wave is assumed to propagate to the right ($c > 0$). If the wave is propagating to the left ($c < 0$), the upwind-biased scheme uses more stencil points from the right than those from the left, for example, a fourth-order, seven-point stencil upwind DRP scheme with $M=4$ and $N=2$ for $c<0$. The coefficients of the DRP scheme for $c<0$ can be derived directly from its corresponding counterpart for $c>0$ if the same number of stencil points and the same fashion of bias are used. The effective wave number $\bar{\alpha}$ of the scheme with coefficients a_j^{MN} is the conjugate of that of the scheme with coefficients a_j^{NM}. The opposite sign in the imaginary part of the effective wave number $\bar{\alpha}$ of the scheme is needed to ensure the stability for waves propagating in two contrary directions. In Fig. 1, the Fourier analysis of the two fourth-order, seven-point stencil optimized upwind DRP schemes ($M=2$, $N=4$) with $\beta_0 = \pi/2$ and $\pi/3$ is shown along with other well-known schemes. The parameters λ and σ are considered as $\lambda = 0.0374$ and $\sigma = 0.2675\pi$ for both of the optimized upwind schemes. Results shown in Fig. 1 indicate that the optimized upwind scheme with $\beta_0 = \pi/2$ has much less dispersion and dissipation errors than those of the traditional sixth-order, seven-point stencil upwind scheme ($M=2$, $N=4$). In addition, the two optimized upwind schemes, while keeping the dissipation error minimum, are able to resolve the waves with wave numbers as high as those resolved by Tam and Webb's fourth-order, seven-point stencil central DRP scheme.[4] It can also be seen from Fig. 1 that the deviation from the exact solution increases for both the real and the imaginary parts of the numerical wave number as the range of wave numbers for optimization decreases. In fact, the optimized upwind scheme with $\beta_0 = \pi/3$ has a larger dissipation error than that of the corresponding traditional upwind scheme. Decreasing the range of wave number for optimization alone does not always improve the scheme. To improve the optimized upwind scheme with $\beta_0 = \pi/3$, one has to search for optimum values of parameters λ and σ. Figure 2, which presents the grid resolution requirement in terms of the amplitude error and the phase error, allows us to compare different schemes from another perspective. In Fig. 2, the maximum global amplitude and phase errors are given as 10%. Between the two optimized upwind schemes, results show that the scheme with $\beta_0 = \pi/2$ gives a larger phase error after a wave has traveled

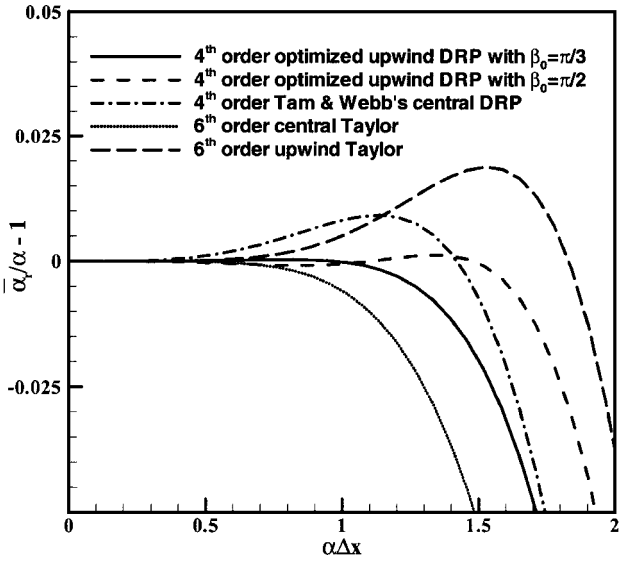

a) Real part

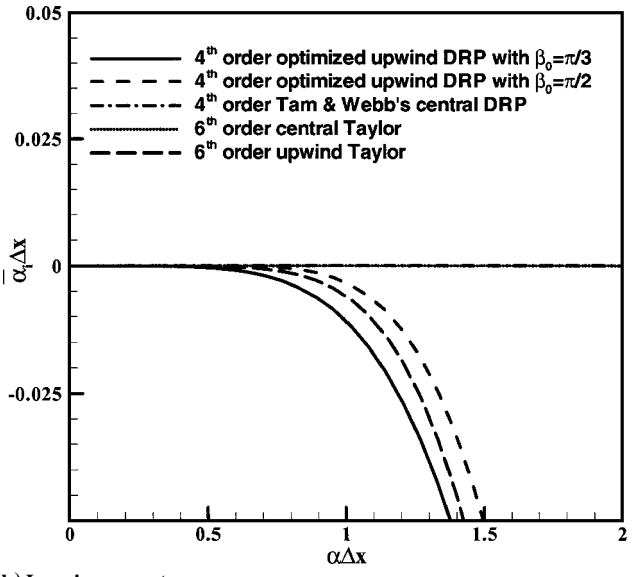

b) Imaginary part

Fig. 1 Effective numerical wave number vs actual wave number for various schemes.

a distance of about 20 wavelengths, and the scheme with $\beta_0 = \pi/3$ yields a larger amplitude error. From Fig. 2, we can also see the grid resolution requirements for Tam and Webb's[4] central DRP scheme and the sixth-order traditional upwind ($M=2$, $N=4$) and central schemes. Because the optimized schemes are optimized for a given range of wave number, they require fewer PPW if the propagation distance is relatively short. As the number of wavelength traveled increases, the advantage of the optimized schemes diminishes as the required PPW increases. The traditional sixth-order upwind scheme, therefore, shows better characteristics (Fig. 2a). However, if fewer PPW are required, the use of optimized schemes not only gives most accurate results but also results in significant savings of the CPU time for realistic multi-dimensional acoustic calculations. For the optimized upwind schemes, the quality of the schemes depends on the optimization range of wave number, the weighting parameter λ, and the control parameter σ. Further investigations of the effects of these parameters on the optimized upwind schemes are expected.[11] For the current investigation, the fourth-order, seven-point stencil optimized upwind scheme with the parameters chosen as $\beta_0 = \pi/2$, $\lambda = 0.0374$, and $\sigma = 0.2675\pi$ is used. The coefficients a_j for this seven-point stencil optimized upwind scheme are given in Table 1. The scheme with coefficients listed in Table 1 are used for calculations of the interior points of a computational domain. For boundaries, the optimized one-side biased spatial finite difference

Table 1 Coefficients for the seven-point stencil optimized upwind scheme with $\beta_0 = \pi/2$

Coefficient	$N=4, M=2, c>0$	Coefficient	$N=2, M=4, c<0$
a_{-4}^{42}	0.161404967151E−01	a_{-2}^{24}	0.4121453788895E−01
a_{-3}^{42}	−0.122821279020E+00	a_{-1}^{24}	−0.4399321927296E+00
a_{-2}^{42}	0.455332277706E+00	a_{0}^{24}	−0.5018904380193E+00
a_{-1}^{42}	−0.12492595882615E+01	a_{1}^{24}	0.12492595882615E+01
a_{0}^{42}	0.5018904380193E+00	a_{2}^{24}	−0.455332277706E+00
a_{1}^{42}	0.4399321927296E+00	a_{3}^{24}	0.122821279020E+00
a_{2}^{42}	−0.4121453788895E−01	a_{4}^{24}	−0.161404967151E−01

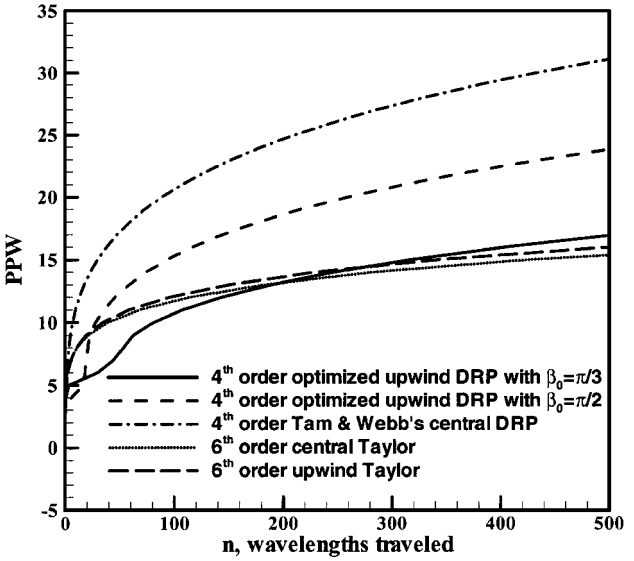

a) Maximum global phase error <10%

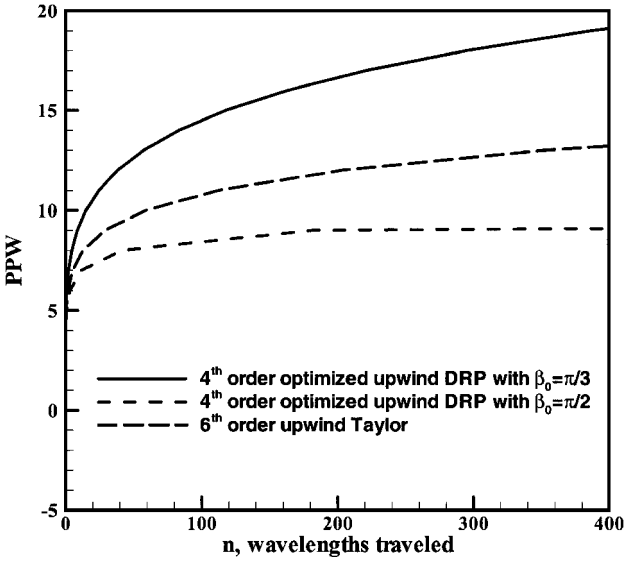

b) Maximum global amplitude error <10%

Fig. 2 Grid resolution requirement for various schemes.

schemes are used. The coefficients for the seven-point stencil one-side biased schemes are given in Table 2. It is noted that coefficients a_j^{60} are obtained solely from the Taylor series expansion. The reason for choosing the coefficients a_j^{60} solely based on the Taylor series expansion is that the optimization did not make a visible improvement. Note that $a_{-j}^{MN} = -a_j^{NM}$. The optimized upwind schemes described here are implemented to solve the three-dimensional acoustic field equations in a general curvilinear coordinate system.[12] The procedures are identical with those used for any traditional upwind schemes. The flux vector splitting method is used, and the Jacobian matrices are split according to positive or negative eigenvalues.

Table 2 Coefficients for the seven-point stencil one-side biased schemes for boundaries with $\beta_0 = \pi/2$

Coefficient	$N=5, M=1$	Coefficient	$N=6, M=0$
a_{-5}^{51}	−0.306489732244242E−01	a_{-6}^{60}	1/6
a_{-4}^{51}	0.202225858313369E+00	a_{-5}^{60}	−6/5
a_{-3}^{51}	−0.634728026533812E+00	a_{-4}^{60}	15/4
a_{-2}^{51}	0.12962996541567 1E+01	a_{-3}^{60}	−20/3
a_{-1}^{51}	−0.214305478803459E+01	a_{-2}^{60}	15/2
a_{0}^{51}	0.110888726751399E+01	a_{-1}^{60}	−6
a_{1}^{51}	0.201019007808754E+00	a_{0}^{60}	49/20

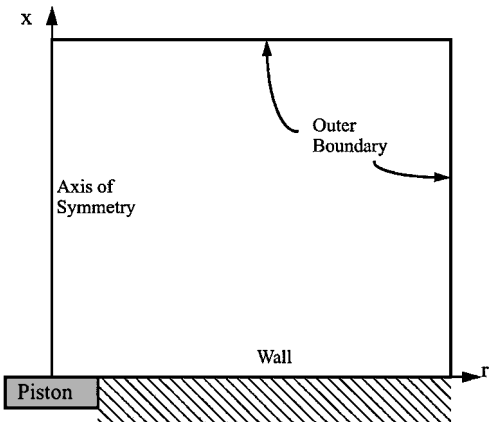

Fig. 3 Schematics of computational domain for acoustic radiation from an oscillating piston.

Applications of High-Order Optimized Upwind DRP Scheme

To validate the effectiveness of the fourth-order, seven-point stencil optimized upwind scheme, a series of numerical simulations has been carried out for various acoustic wave propagation problems. Analytical solutions are also calculated for validating of the numerical results. Results from the optimized upwind DRP scheme are compared with those from Tam and Webb's fourth-order, seven-point stencil central DRP scheme.[4] Furthermore, in all of the simulations, the temporal difference scheme from Tam and Webb[4] is used.

Acoustic Radiation from an Oscillating Piston

Acoustic radiation from an oscillating circular piston in a wall (Fig. 3) is considered to validate the accuracy and the robustness of the optimized upwind DRP scheme in two dimensions in the presence of solid wall boundary conditions. A cylindrical coordinate system originated at the center of the piston is used. The radius of the piston is given as 10. The computational domain is defined as $0 \le x \le 100$ and $0 \le r \le 100$. With axisymmetry, the governing two-dimensional Euler equations can be written as

$$\frac{\partial u}{\partial t} + \frac{\partial p}{\partial x} = 0 \tag{5}$$

$$\frac{\partial v}{\partial t} + \frac{\partial p}{\partial r} = 0 \tag{6}$$

$$\frac{\partial p}{\partial t} + \frac{\partial v}{\partial r} + \frac{v}{r} + \frac{\partial u}{\partial x} = 0 \tag{7}$$

where u and v are the velocity components in the x and r directions, respectively. The piston is oscillating with a speed of $u = 10^{-4}\sin(\pi t/5)$. The grid sizes Δx and Δr are both given as 1. The boundary conditions on the wall surface ($x = 0$) are $u = 0$ for $r \geq R$ (where R is the radius of the piston) and $u = 10^{-4}\sin(\pi t/5)$ for $r < R$. Therefore, the derivatives of pressure along the direction normal to the wall are given as

$$\frac{\partial p}{\partial x} = \begin{cases} (10^{-4}\pi t/5)\cos(\pi t/5), & 0 \leq r < R \\ (10^{-4}\pi t/10)\cos(\pi t/5), & r = R \\ 0, & r > R \end{cases} \tag{8}$$

The boundary conditions on the solid wall are implemented by adding a layer of ghost cells next to the solid wall.[13] At the axis of symmetry, $r = 0$, we have the pressure gradient boundary condition $\partial p/\partial r = 0$; the implementation of this boundary condition is identical with that of solid wall boundary conditions. In addition, at the axis of symmetry, Eq. (7) becomes singular. The term v/r in Eq. (7) is replaced by $\partial v/\partial r$ because $v/r \to \partial v/\partial r$ as $r \to 0$ and $v \to 0$. Radiation boundary conditions[4] are imposed at the top and the right boundaries of the computational domain. The initial condition is given as $\rho = u = v = p = 0$. After the initial disturbance has propagated out of the computational domain, the solution becomes a periodic sinusoidal wave with a cycle of the piston oscillation as its period. Figures 4 and 5 show the pressure contours obtained with the optimized upwind scheme and Tam and Webb's central DRP (without damping) at the beginning of a cycle.[4] The contours

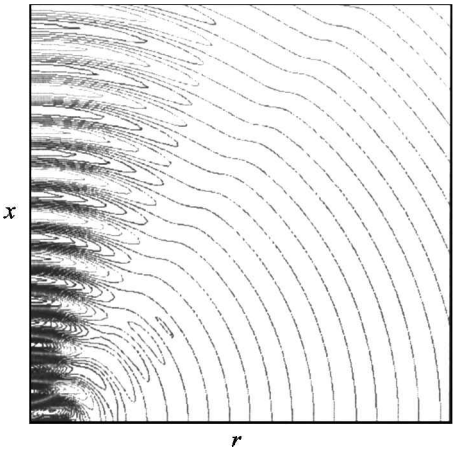

Fig. 4 Pressure contours at the beginning of a cycle using the optimized upwind scheme.

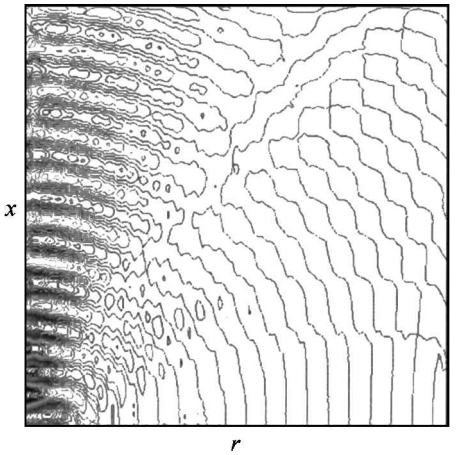

Fig. 5 Pressure contours at the beginning of a cycle using Tam and Webb's central DRP scheme without damping.[4]

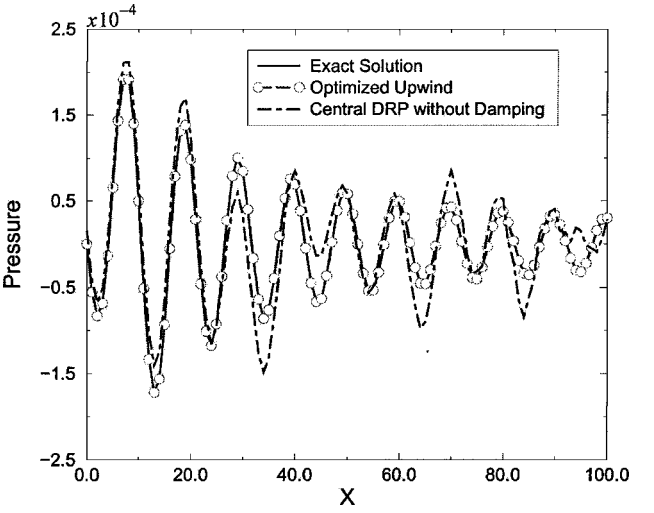

Fig. 6 Pressure distribution along the axis of symmetry at the beginning of a cycle.

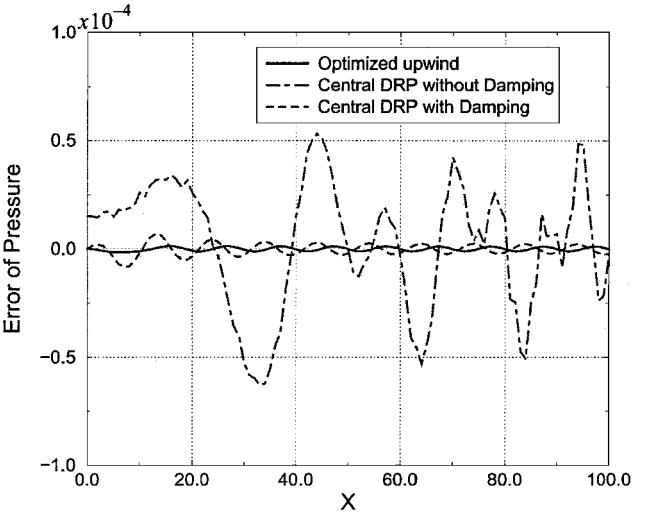

Fig. 7 Numerical error for the pressure along the axis of symmetry at the beginning of a cycle.

obtained by the optimized upwind scheme would have been indistinguishable from those of the exact solution if we had plotted them in the same graph. However, the pressure contours obtained with the central DRP scheme without damping have seriously spurious oscillations. A comparison of the pressure distributions along the axis of symmetry at the beginning of a cycle is given in Fig. 6. It is shown that the pressure obtained with the optimized upwind scheme agrees very well with the exact solution, and the pressure obtained with the central DRP without damping deviates from the exact solution. This deviation increases as the time increases until the solution is deteriorated. It is well known that for the central DRP scheme, an artificial damping term is needed to eliminate the spurious oscillations. However, the damping coefficients are determined by trial and error. A fine tuning may be required to get good results. Here we follow the approach of Tam et al.[14] and use the same damping coefficients, that is, an artificial mesh Reynolds number of 5. With the inclusion of the artificial damping terms, spurious waves are effectively eliminated from the numerical solution.

Figure 7 shows the comparisons of the numerical error for the pressure between the optimized upwind scheme and the central DRP scheme with and without artificial damping. Results shown in Fig. 7 demonstrate that the error associated with the optimized upwind scheme is significantly less than that associated with the central DRP scheme without damping and is slightly less than that of the central DRP scheme with carefully tuned damping coefficients. The results also verify that the optimized upwind scheme minimizes not

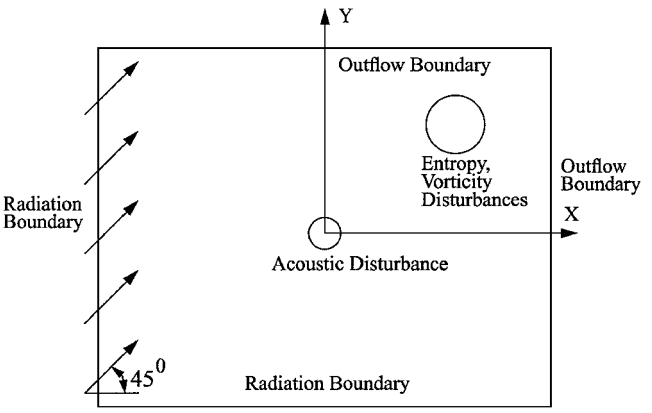

Fig. 8 Schematics of computational domain and boundary and initial conditions for acoustic propagation in a two-dimensional uniform flow.

only the dispersion error but also the dissipation error. In addition, one of the important features of the optimized upwind schemes is that it applies a different amount of minimum dissipation to each variable. The CPU time that required for the optimized upwind scheme is about the same as that for the central DRP scheme with artificial damping.

Acoustic Wave Propagation in a Two-Dimensional Uniform Flow

The second acoustic problem we used to verify the optimized upwind scheme is one with a mean flow. In this problem, acoustic, entropy, and vorticity disturbances are initially released at different locations with a uniform mean flow of a freestream Mach number 0.5. The computational domain, the boundary conditions, the locations of the initial disturbances, and the direction of the mean flow are given schematically in Fig. 8. The specific functions of the initial disturbances are given as

$$\rho(x, y) = \exp\{-\ln 2[(x^2 + y^2)/9]\} + 0.1\exp(-\ln 2\{[(x-67)^2 + (y-67)^2]/25\}) \quad (9)$$

$$u(x, y) = 0.04(y-67)\exp(-\ln 2\{[(x-67)^2 + (y-67)^2]/25\}) \quad (10)$$

$$v(x, y) = -0.04(x-67)\exp(-\ln 2\{[(x-67)^2 + (y-67)^2]/25\}) \quad (11)$$

$$p(x, y) = \exp\{-\ln 2[(x^2 + y^2)/9]\} \quad (12)$$

It is seen that the acoustic disturbance is released initially at the origin of the coordinate system. The acoustic disturbance propagates at the speed of sound relative to the mean flow. The entropy and vorticity disturbances are released initially at (67,67). They propagate at the speed of the mean flow. The computational domain is given as $-100 \le x \le 100$ and $-100 \le y \le 100$. The grid sizes Δx and Δy are set to be 1. Radiation boundary conditions[4] are imposed at the left and bottom boundaries where there is an inflow. Outflow boundary conditions[4] are used on the right and the top boundaries. Figure 9 shows the density surface plot calculated with the optimized upwind scheme at time $t = 80$. It shows that the acoustic disturbance catches up and interacts with the entropy and vorticity disturbances and propagates partially out of the computational domain. Note that no visible reflections near the boundaries are observed in Fig. 9. The density distribution along the direction of the diagonal of the computational domain ($x = y$) is calculated at $t = 80$ using the optimized upwind DRP scheme and the central DRP scheme without damping.

A comparison of the numerical density distributions with the exact solution is made in Fig. 10. The blip in the density results by the central DRP scheme is because the Euler equations are solved instead of the linearized Euler equations in the program code. Results shown on Fig. 10 indicate that the solutions from both numerical

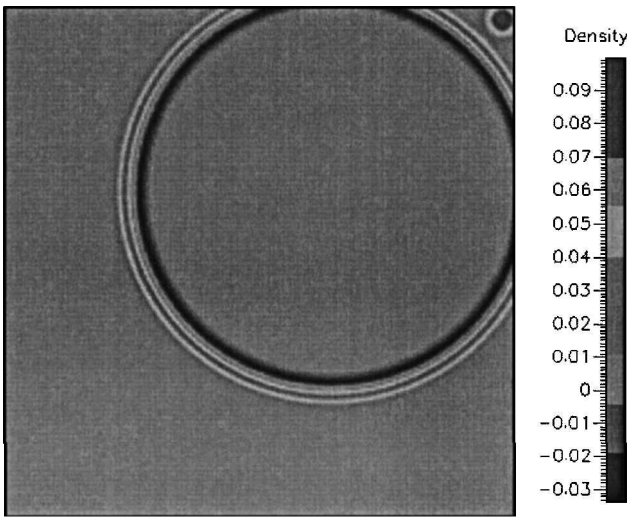

Fig. 9 Contour plot of density perturbations using the optimized upwind scheme at $t = 80$.

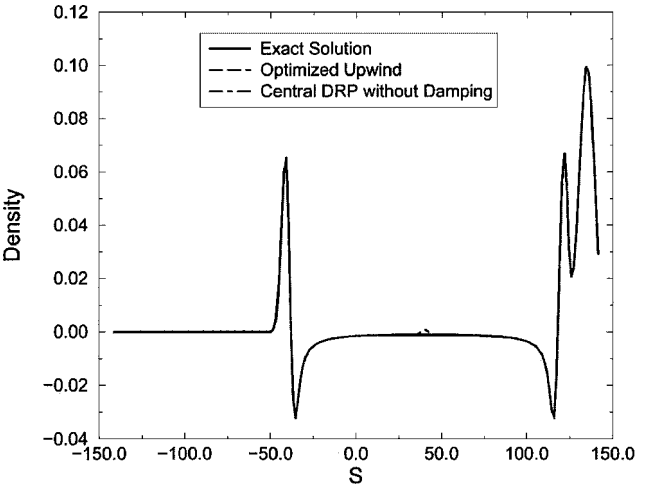

Fig. 10 Density perturbation along the line $y = x$ at $t = 80$.

schemes agree well with the analytical solution. However, Fig. 11 shows that the error generated by the optimized upwind scheme is significantly less than that generated by the central DRP scheme at peak values of the density because the dissipation error of the optimized upwind scheme is minimized by the optimization.

Acoustic Scattering by a Sphere

Unlike the previous applications that are limited to two-dimensional acoustic problems with straight boundaries, the third problem is chosen to study the behaviors of the optimized upwind scheme in the presence of a curved three-dimensional object, a sphere. A schematic diagram of the problem of acoustic scattering by a sphere is given in Fig. 12. Although the physical phenomenon of the scattering is well understood, three-dimensional simulations of such problem with a moderate to high frequency remain as a challenging task because of the number of grid points per wavelength needed to resolve the acoustic waves. In addition, the numerical schemes have to be implemented with spherical-shape curved boundaries. Previously, this acoustic scattering problem was solved in Cartesian grids with the utilization of parallel computation.[15] For a two-dimensional acoustic problem in the presence of a circular geometry, it has been shown[2,5] that the numerical solutions from the DRP schemes agree very well with the analytical solutions. In the current study, the spherical coordinate system is considered. The computation is carried out with the spherical coordinate transform

$$x = r\sin\theta\cos\varphi, \qquad y = r\sin\theta\sin\varphi, \qquad z = r\cos\theta \quad (13)$$

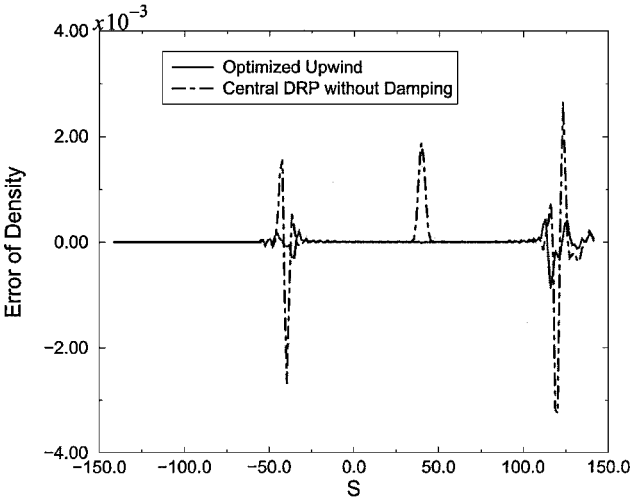

Fig. 11 Numerical error for the density along the line $y = x$ at $t = 80$.

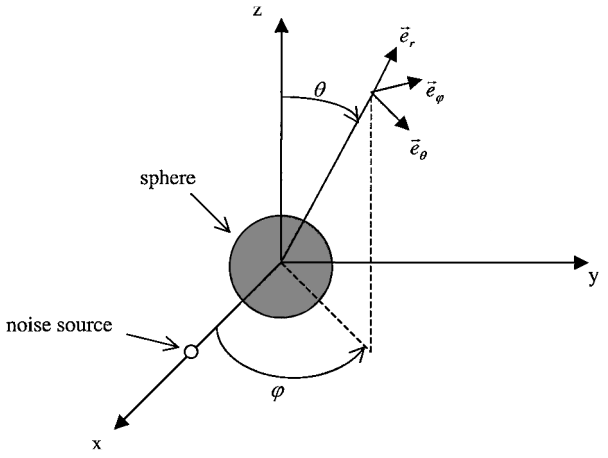

Fig. 12 Schematic diagram of acoustic scattering by a sphere.

The governing linearized Euler equations with the Cartesian variable vector $\boldsymbol{q} = (\rho, u, v, w, p)^T$ as the dependent variable vector are given by

$$\frac{\partial \boldsymbol{q}}{\partial t} + \tilde{A}_0 \frac{\partial \boldsymbol{q}}{\partial r} + \tilde{B}_0 \frac{\partial \boldsymbol{q}}{\partial \theta} + \tilde{C}_0 \frac{\partial \boldsymbol{q}}{\partial \varphi} = \boldsymbol{S} \tag{14}$$

with

$$\tilde{A}_0 = A_0 \sin\theta \cos\varphi + B_0 \sin\theta \sin\varphi + C_0 \cos\theta \tag{15}$$

$$\tilde{B}_0 = (1/r)[A_0 \cos\theta \cos\varphi + B_0 \cos\theta \sin\varphi - C_0 \sin\theta] \tag{16}$$

$$\tilde{C}_0 = 1/r \sin\theta[-A_0 \sin\varphi + B_0 \cos\varphi] \tag{17}$$

where A_0, B_0, and C_0 are the corresponding Jacobian matrices from the Cartesian coordinate system.[12] The source vector $\boldsymbol{S}$ is given as $\boldsymbol{S} = (0, 0, 0, 0, s)$ with

$$s = 0.01 \exp\{-16(\ell n 2)\lfloor (x-2)^2 + y^2 + z^2 \rfloor\} \cos(2\pi t) \tag{18}$$

when the properties of symmetry are used, only the region bounded by $0 \le \theta \le \pi/2$ and $0 \le \varphi \le \pi$ is needed for the simulation. We can see that, after the coordinate transformation, the three-dimensional acoustic field equation (14) becomes singular at the pole (where $\theta = 0$). Special treatments for the grid points near the pole are needed for the numerical stability. Instead of using the spherical coordinate system, the Cartesian coordinate system is used at the pole. The derivatives are evaluated at the pole by the following:

$$\frac{\partial \boldsymbol{q}}{\partial x} = \frac{1}{r} \frac{\partial \boldsymbol{q}}{\partial \theta}\bigg|_{\varphi=0}, \qquad \frac{\partial \boldsymbol{q}}{\partial y} = \frac{1}{r} \frac{\partial \boldsymbol{q}}{\partial \theta}\bigg|_{\varphi=\pi/2}, \qquad \frac{\partial \boldsymbol{q}}{\partial z} = \frac{\partial \boldsymbol{q}}{\partial r} \tag{19}$$

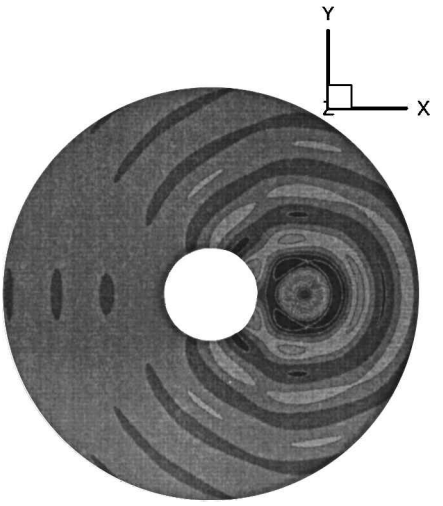

Fig. 13 Pressure contours at the beginning of a period along the plane $z = 0$.

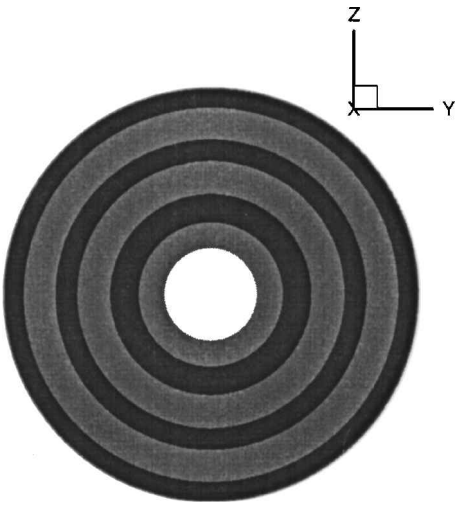

Fig. 14 Pressure contours at the beginning of a period along the plane $x = 0$.

where the subscripts denote the planes that are used to evaluate the derivatives. Because the grids are skewed near the pole, it imposes a very strict limit on the time step. In the calculation, the values of acoustic variables in the first three levels of grid points next to the pole are obtained by a third-order-accurate interpolation of the values at the pole and the values at the fourth and fifth levels of grid points next to the pole. A grid system of $80 \times 60 \times 90$ points with $\Delta r = 3.5D/80$ (where D is the diameter of the sphere), $\Delta\theta = 1.5$ deg, and $\Delta\varphi = 2$ deg is used. The time step is given as 0.0005. Contours of instantaneous pressure at the beginning of a period are plotted in Fig. 13 along the plane $z = 0$ and in Fig. 14 along the plane $x = 0$. Results in Fig. 13 show the radiation waves, reflected waves, and the interaction of waves and the sphere. The concentric pattern of the pressure shown in Fig. 14 clearly demonstrates that the physical phenomenon is reproduced successfully by the simulations. The fact that there are no noticeable differences in the wave pattern near the pole validates the treatments for the grid points near the pole.

Quantitative comparisons of the numerical results with the analytic solutions[16] are shown in Fig. 15 along the line at $y = 0$ and $z = 0$ and in Fig. 16 along the line at $x = 0$ and $z = 0$. The small discrepancies near the vicinity of the sphere could be caused by the use of a relative coarse grid. Furthermore, because there is a scaling factor between the numerical and the analytical solutions, the discrepancies near the sphere can be reduced, whereas the errors between the numerical and the analytical solutions away from the sphere increases slightly. A good agreement between the numerical and the

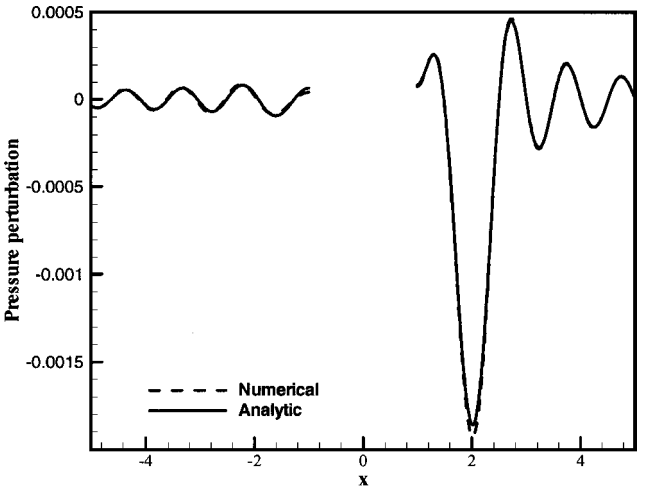

Fig. 15 Comparison of the numerical and the analytic solutions of the scattered acoustic field along the line at $y = 0$ and $z = 0$.

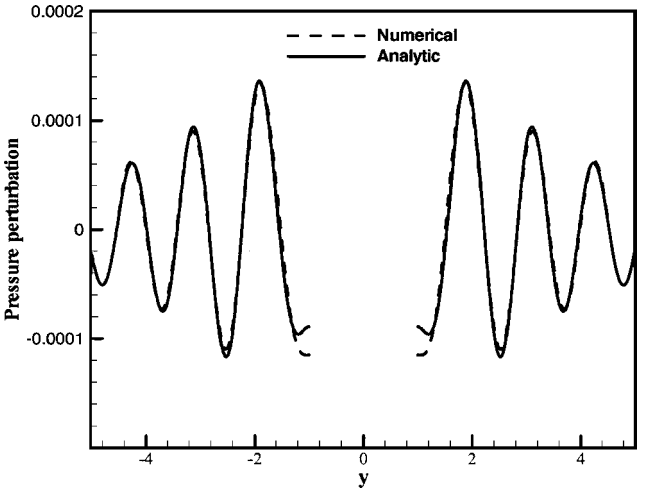

Fig. 16 Comparison of the numerical and the analytic solutions of the scattered acoustic field along the line at $x = 0$ and $z = 0$.

analytical solutions has been observed for this three-dimensional acoustic scattering problem.

Conclusions

The optimized upwind schemes have been studied and implemented to multidimensional acoustic problems. A series of acoustic wave propagation problems with various boundary conditions, such as solid walls, radiation and outflow, is solved using the optimized upwind schemes. The numerical results have verified the accuracy and the effectiveness of the optimized upwind schemes and have demonstrated that the optimized upwind schemes minimizes not only the dispersion error but also the dissipation error while retaining the numerical stability. The computational grid and the time step are kept the same for the different numerical schemes. The results show that the optimized upwind scheme damps out the spurious short waves automatically without the need of filter or explicit dissipation terms. The results of the acoustic radiation from an oscillating piston clearly demonstrate that the computational error from the optimized upwind scheme is significantly less than that from the central DRP scheme without damping and is comparable to that from the central DRP scheme with damping. However, a fine tuning may be required for the central DRP scheme with damping. A good agreement between the numerical and the analytical solutions for a three-dimensional calculation of acoustic scattering by a sphere shows that the optimized upwind schemes can be used to solve acoustic wave propagation problems in the presence of curved boundaries. Therefore, the schemes may have the potential to solve acoustic problems with a relatively complex geometry.

Acknowledgment

We would like to thank P. J. Morris for providing the analytic solution of the acoustic scattering problem.

References

[1]Tam, C. K. W., "Computational Aeroacoustics: Issues and Methods," *AIAA Journal*, Vol. 33, No. 10, 1995, pp. 1788–1796.

[2]Hardin, J. C., Ristorcelli, J. R., and Tam, C. K. W., *ICASE/LaRC Workshop on Benchmark Problems in Computational Aeroacoustics*, NASA CP-3300, May 1995.

[3]Hixon, R., "Evaluation of a High-Accuracy MacCormack-Type Scheme Using Benchmark Problems," NASA CR 202324, ICOMP-97-03, 1997.

[4]Tam, C. K. W., and Webb, J. C., "Dispersion-Relation-Preserving Finite Difference Schemes for Computational Acoustics," *Journal Computational Physics*, Vol. 107, No. 2, 1993, pp. 262–281.

[5]Lockard, D. P., Brentner, K. S., and Atkins, H. L., "High-Accuracy Algorithms for Computational Aeroacoustics," *AIAA Journal*, Vol. 33, No. 2, 1995, pp. 246–251.

[6]Li, Y., "Wavenumber-Extended High-Order Upwind-Biased Finite Difference Schemes for Convective Scalar Transport," *Journal of Computational Physics*, Vol. 133, 1997, pp. 235–255.

[7]Zhuang, M., and Chen, R. F., "Optimized Upwind Dispersion-Relation-Preserving Finite Difference Schemes for Computational Aeroacoustics," *AIAA Journal*, Vol. 36, No. 11, 1998, pp. 2146–2148.

[8]Warming, R. F., and Beam, R. M., "Upwind Second-Order Difference Schemes and Applications in Unsteady Aerodynamic Flows," *Proceedings of the 2nd AIAA Computational Fluid Dynamics Conference*, AIAA, New York, 1975, pp. 17–28.

[9]Anderson, D. A., Tannehill, J. C., and Pletcher, R. H., *Computational Fluid Mechanics and Heat Transfer*, Taylor and Francis, Washington, DC, 1984.

[10]Barth, T. J., "Higher Order Solution of the Euler Equations on Unstructured Grids Using Quadratic Reconstruction," AIAA Paper 90-0013, 1990.

[11]Zheng, S., and Zhuang, M., "High-Order Optimized Numerical Schemes for Computational Aeroacoustics," *Proceedings of the 2001 ASME International Mechanical Engineering Congress and Exposition on Noise Control and Acoustics*, American Society for Mechanical Engineers, New York, 2001, pp. 261–270.

[12]Chen, R. F., "Study on Optimized Upwind Schemes for Computational Aeroacoustics and Extension of a Fully Conservative Chimera to Finite Difference Schmes," Ph.D. Dissertation, Dept. of Mechanical Engineering, Michigan State Univ., East Lansing, MI, Nov. 1998.

[13]Tam, C. K. W., and Dong, Z., "Wall Boundary Conditions for High-Order Finite Difference Schemes in Computational Aeroacoustics," *Theorectical and Computational Fluid Dynamics*, Vol. 6, No. 6, 1994, pp. 303–322.

[14]Tam, C. K. W., Shen, H., Kurbatskii, K. A., Auriault, L., Dong, Z., and Webb, J. C., "Solutions of the Benchmark Problems by the Dispersion-Relation-Preserving Scheme," *Proceedings of the 1st Computational Aeroacoustics Workshop on Benchmark Problems*, NASA CP-3300, 1995, pp. 149–171.

[15]Shieh, C. M., and Morris, P. J., "Three-Dimensional Calculations of Acoustic Scattering by a Sphere: A Parallel Implementation," *Proceedings of the 2nd Computational Aeroacoustics Workshop on Benchmark Problems*, NASA CP-3352, 1997, pp. 241–246.

[16]Morris, P. J., "Scattering of Sound from a Spatially Distributed, Spherically Symmetric Source by a Sphere," *Journal of the Acoustical Society of America*, Vol. 98, 1995, pp. 3536–3539.

P. J. Morris
Associate Editor